

PAPER

Phase field modeling of the effect of porosity on grain growth kinetics in polycrystalline ceramics

To cite this article: K Ahmed *et al* 2013 *Modelling Simul. Mater. Sci. Eng.* **21** 065005

View the [article online](#) for updates and enhancements.

Related content

- [Phase-field modeling of pores and precipitates in polycrystalline systems](#)
Julia Kundin, Hassan Sohaib, Raphael Schiedung *et al.*
- [Phase field modeling of void nucleation and growth in irradiated metals](#)
Srujan Rokkam, Anter El-Azab, Paul Millett *et al.*
- [Friction pressure method for simulating solute drag and particle pinning in a multiphase-field model](#)
S Shahandeh, M Greenwood and M Militzer

Recent citations

- [Influence of bulk free energy density on single void evolution based on the phase-field method](#)
Yang Li *et al*
- [Numerical Simulation of Dendrite Growth and Micro Segregation of Ni-Cu Alloy](#)
Ming Guang Wang and Shan Jiang
- [Phase field study the effects of interfacial energy anisotropy on the thermal migration of voids](#)
W.J. Chen *et al*



IOP | ebooks™

Bringing you innovative digital publishing with leading voices to create your essential collection of books in STEM research.

Start exploring the collection - download the first chapter of every title for free.

Phase field modeling of the effect of porosity on grain growth kinetics in polycrystalline ceramics

K Ahmed¹, C A Yablinsky², A Schulte², T Allen² and A El-Azab¹

¹ School of Nuclear Engineering, Purdue University, West Lafayette, IN 47907, USA

² College of Engineering, University of Wisconsin-Madison, Madison, WI 53706, USA

E-mail: aelazab@purdue.edu

Received 13 December 2012, in final form 1 May 2013

Published 18 July 2013

Online at stacks.iop.org/MSMSE/21/065005

Abstract

We present a phase field model for investigating grain growth in polycrystalline ceramics containing porosity. Grain growth in such materials is complicated by the interaction between the pores and the grain boundaries, which tends to hinder the kinetics of grain growth. In addition to grain-boundary migration, the model takes into consideration pore-surface diffusion and, whenever effective, other diffusion mechanisms such as volume diffusion and grain-boundary diffusion. The pore-surface diffusion controls the pore mobility. A direct relationship between the model parameters and the material properties is established, which facilitates the quantitative analysis of grain growth. The model is used to investigate the conditions under which porosity is effective in controlling grain growth. Application of the model to ceria shows that grain growth law in this material is sensitive to the level of porosity. In particular, the grain growth in ceria gradually changes from boundary controlled growth to pore controlled growth as porosity increases. The effects of porosity, temperature, grain boundary and surface mobility on grain growth were investigated. The model results agree well with published grain growth experiments.

1. Introduction

It is well established that grain growth takes place in polycrystalline solids at sufficiently high temperature [1–3]. During grain growth the average grain size of a polycrystalline solid increases, which, due to mass conservation, must be accompanied by reduction in the number of grains. During grain growth, the large grains become larger at the expense of small grains. The driving force for grain growth is the decrease in the free energy on account of the reduction in the total grain-boundary area. Grain growth in pure materials was first modeled by Burke and Turnbull more than half a century ago [2]. In that model, they suggested that grain growth proceeds by mass transport of atoms across the grain boundary due to the difference in chemical potential arising from the curvature of the boundary. Following that concept, they

derived the well-known parabolic grain growth law. Later, many computational models were proposed to simulate the grain growth process. The most common of these models are the Monte Carlo Potts model [4–8], front tracking methods [9, 10], vertex models [11–15], cellular automata [16, 17] and phase field models [18–22]. For ideal grain growth in pure materials, these models, in spite of their differences, reach the same conclusions that were reached by Burke and Turnbull on kinetics of grain growth [2]. In particular, these models confirm that parabolic growth law and the existence of time-independent grain size distribution in the scaling regime.

Experimental studies of grain growth in many polycrystalline materials showed deviations from the parabolic growth kinetics [1]. Such deviations were attributed to the presence of second phase particles, dopants or impurities, inclusions and pores. The presence of such features exerts a drag force on the grain boundary that retards the grain growth kinetics. The effects of particles and pores on grain growth kinetics received much attention. For example, some theoretical models were proposed to investigate the so-called particle-inhibited grain growth [1]. These models can be classified into two categories depending on whether the particles are treated as mobile or immobile. Zener was the first to quantitatively study particle-inhibited grain growth [1]. He considered the particles to be immobile, spherical, mono-size, insoluble and randomly distributed in the polycrystalline solid. A key result of his analysis is the existence of limiting grain size at which the growth process ceases. This limiting grain size is proportional to the particle size and inversely proportional to the particle volume fraction. Computational techniques such as Monte Carlo [23, 24] and phase field [25] models confirmed Zener's findings.

In comparison with the case of immobile particles, the effect of mobile particles or pores on the microstructure evolution of polycrystalline solids during the grain growth is more complex [1]. For example, it is well established that the microstructure evolution and the grain growth kinetics of porous ceramics are strongly dependent on the interaction between the grain boundaries and pores [1, 3]. The interaction between pores and grain boundaries in porous ceramics is affected by thermodynamic factors such as surface and grain-boundary energies that define the equilibrium dihedral angle. It is also influenced by kinetic factors such as the pore versus grain-boundary mobility, which determine whether the pore will be attached to or separated from the grain boundary during the movement of the latter. Since the equilibrium dihedral angle must be maintained, increase in the amount of porosity can strongly hinder grain-boundary migration. This could render the grain growth process energetically unfavorable unless it is assisted by other processes that lower this energy barrier. Mass transport mechanisms such as surface, lattice and grain-boundary diffusion were proposed as mechanisms that facilitate grain growth [1, 26].

In this communication, we present an elaborate phase field model for grain growth in porous polycrystalline solids. Different mass transport mechanisms are accounted for in this model in order to track the microstructure evolution while correctly capturing all relevant kinetics. In addition to grain-boundary motion and pore-surface diffusion, which are the main mechanisms, grain boundary and lattice diffusion were also considered. A direct relationship between the free energy and kinetic parameters of the phase field model and the physical properties of the polycrystalline system has been established. This physical underpinning of the model parameters, which distinguishes the current model from the majority of existing ones, enables us to apply the model to actual materials. We apply the model to the case of grain growth in ceria, which is a good surrogate material for uranium dioxide. Ceria has also been chosen due to its technological importance in catalysis, sensors and fuel cell technologies [27, 28].

2. Phase field model

As mentioned earlier, the grain growth in a pure, porous ceramic is carried by two main mechanisms, the motion of grain boundaries and mass transport by diffusion along the pore surface. In certain situations, especially in the presence of porosity, mass transport through the bulk and along grain boundaries might also contribute to the evolution kinetics. A desirable model feature will thus include all these mechanisms, which is followed here. The phase field model relies on resolving all features in the material. When all of the above mechanisms are working, both conserved and non-conserved phase field variables are used. The conserved variable, $\rho(r, t)$, represents the fractional density of the solid and it is taken to be 1 in the solid phase and 0 in the pore region. Non-conserved phase field variables, $\eta_\alpha(r, t)$, $\alpha = 1, 2, \dots, p$, are used to distinguish different grains, assumed here to have different crystallographic orientations, such that η_α equals 1 in α th grain and 0 otherwise. Here, p is the total number of grains in the solid region under consideration. Since these variables vary slowly in bulk or pore regions and rapidly across the interface between these regions, their evolution gives the position of interfaces as a function of time and hence reveals the time evolution of microstructure.

In order to derive the kinetic equations of phase field variables, the free energy of the system must be given in terms of the phase field variables. Here the free energy functional of the system is assumed to have the form

$$F = \int \left[f(\rho, \eta_\alpha) + \frac{1}{2} \kappa_\rho |\nabla \rho|^2 + \frac{1}{2} \sum_{\alpha=1}^p \kappa_{\eta_\alpha} |\nabla \eta_\alpha|^2 \right] d^3 r, \quad (1)$$

where the first term represents the bulk (homogeneous) free energy density and the gradient terms give the energy contribution from free surfaces and grain boundaries, respectively. The gradient coefficients κ_ρ and κ_{η_α} are material constants to be determined in terms of other measurable materials parameters. Usually, the homogeneous free energy term represents the equilibrium free energy density that defines coexistence of phases. In the present case, that term represents the division of the material into pore versus solid phases. A particular form for the bulk free energy is a Landau-type polynomial expansion in terms of the phase field variables [29]. Here we adopt a form that was suggested by Wang [30] to simulate the sintering of powder compact,

$$f(\rho, \eta_\alpha) = B\rho^2(1 - \rho)^2 + C \left[\rho^2 + 6(1 - \rho) \sum_{\alpha} \eta_\alpha^2 - 4(2 - \rho) \sum_{\alpha} \eta_\alpha^3 + 3 \left(\sum_{\alpha} \eta_\alpha^2 \right)^2 \right], \quad (2)$$

where B and C are constants. The Landau-type potential of equation (2) is so constructed to give rise to $(p + 1)$ minima, i.e. this form requires the free energy to be a minimum in the pore and in each grain of the solid phase. This particular free energy form was adopted for two reasons. The first is that it is able to capture different stages of sintering including grain growth. The second is the fact that its parameters can be directly related to material properties as established in the [appendix](#).

The kinetic equations for the phase field variables can be obtained straightforwardly. Since the normalized density field is a conserved variable, it evolves according to the continuity equation

$$\frac{\partial \rho}{\partial t} = -\nabla \cdot \mathbf{J}, \quad (3)$$

in which \mathbf{J} is the mass flux, which, according to linear irreversible thermodynamics, is expressed as

$$\mathbf{J} = -\mathbf{M} \nabla \psi, \quad (4)$$

where \mathbf{M} is the chemical mobility tensor and ψ is a generalized chemical potential. This chemical potential is given by the variational derivative of the free energy functional with respect to the conserved phase field variable ρ ,

$$\psi = \frac{\delta F}{\delta \rho} = \frac{\partial f(\rho, \eta_\alpha)}{\partial \rho} - \kappa_\rho \nabla^2 \rho. \quad (5)$$

The scalar chemical mobility is usually related to the diffusion coefficient D by

$$M = \frac{v_m D}{RT}, \quad (6)$$

where v_m is the molar volume, R is the universal gas constant and T is the temperature.

Due to the fact that surface and grain-boundary diffusion is tangential to the surface and grain boundary, respectively, the corresponding mobility (or diffusivity) must be expressed as tensors projecting mass transport onto such interfaces. This tensor form of mobility can be constructed in a way that is consistent with the sharp interface limit [31]. The expression for the surface diffusion tensor \mathbf{D}^s has the form

$$\mathbf{D}^s = D^s \rho^2 (1 - \rho)^2 \mathbf{T}^s, \quad (7)$$

where D^s is the surface diffusivity and \mathbf{T}^s is a surface projection tensor, which guarantees that the surface diffusion is confined along the surface. \mathbf{T}^s has the form

$$\mathbf{T}^s = \mathbf{I} - \mathbf{n}_s \otimes \mathbf{n}_s. \quad (8)$$

In the above, \mathbf{I} is the identity tensor, the symbol \otimes represents the dyadic product and \mathbf{n}_s is the unit normal to the surface, which is given by

$$\mathbf{n}_s = \frac{\nabla \rho}{|\nabla \rho|}. \quad (9)$$

This form makes the surface diffusion tensor \mathbf{D}^s anisotropic with zero eigenvalue in one of the three spatial eigen directions (the one perpendicular to the surface). The function $\rho^2(1 - \rho)^2$ confines that mechanism to the (diffuse) surface region. Similarly, we confine the grain-boundary diffusion along the grain boundaries by constructing the grain-boundary diffusion tensor in the form

$$\mathbf{D}^{\text{gb}} = D^{\text{gb}} \sum_{i=1}^p \sum_{j=1, j \neq i}^p \eta_i \eta_j \mathbf{T}^{\text{gb}}. \quad (10)$$

Again \mathbf{D}^{gb} is the grain-boundary diffusion tensor, D^{gb} is the grain-boundary diffusion coefficient of the material and \mathbf{T}^{gb} is the grain-boundary projection tensor, which guarantees that the grain-boundary diffusion is confined along the grain boundary. This tensor takes on the form

$$\mathbf{T}^{\text{gb}} = \mathbf{I} - \mathbf{n}_{\text{gb}} \otimes \mathbf{n}_{\text{gb}}. \quad (11)$$

In this case, \mathbf{n}_{gb} is the unit normal to the grain boundary. For two neighboring grains, i and j , the latter is given by

$$\mathbf{n}_{\text{gb}} = \frac{\nabla \eta_i - \nabla \eta_j}{|\nabla \eta_i - \nabla \eta_j|}. \quad (12)$$

Finally, the lattice diffusion tensor is constructed as

$$\mathbf{D}^l = D^l \xi(\rho) \mathbf{I}, \quad (13)$$

where D^l is the lattice (volume) diffusion tensor, D^l is the lattice (self-) diffusion coefficient of the material, and $\xi(\rho)$ is a function which guarantees nontrivial values of diffusivity in the solid region and zero values in the pores; this function has the form

$$\xi(\rho) = \rho^3(10 - 15\rho + 6\rho^2). \quad (14)$$

The solid phase is characterized by a mass density of unity making $\xi(\rho) = 1$ in the solid region and 0 in the pores. The above formulation assumes isotropic lattice diffusion since the lattice diffusion tensor is a diagonal matrix with a constant value D^l on the diagonal.

The tensor form of the diffusion coefficients results in similar expressions for the corresponding chemical mobility. The total mobility tensor (the one appearing in equation (4)) is the sum of the surface, grain boundary and lattice mobility tensors, which can be obtained from the corresponding diffusion tensors by means of equation (6), with M and D replaced with their tensor counterparts. By substituting (4) and (5) into (3), and taking into account the fact the chemical mobility is a tensor quantity, we obtain

$$\frac{\partial \rho}{\partial t} = \nabla \cdot \left(M \nabla \frac{\delta F}{\delta \rho} \right). \quad (15)$$

The above equation is the Cahn–Hilliard diffusion equation [32]. The evolution of the non-conserved phase field variables is governed by Allen–Cahn structural relaxation equation [33], which has the form

$$\frac{\partial \eta_\alpha}{\partial t} = -L \frac{\delta F}{\delta \eta_\alpha} = -L \left[\frac{\partial f(\rho, \eta_\alpha)}{\partial \eta_\alpha} - \kappa_{\eta_\alpha} \nabla^2 \eta_\alpha \right]; \quad \alpha = 1, 2 \dots p. \quad (16)$$

L in the above equation is a material constant characterizing the mobility of grain-boundary motion; assuming a constant value of L is consistent with the assumption of isotropic grain growth we follow here. When the mobility of the grain boundary is anisotropic, however, this constant can be turned into a function of the grain-boundary normal. By solving equations (7) and (8) simultaneously, the evolution of the conserved and non-conserved fields can be tracked and the microstructure evolution of the porous polycrystalline solid can be captured.

In order to obtain quantitative results of the microstructure evolution for a given material, the parameters of the free energy functional must be uniquely determined for that material. The Allen–Cahn mobility in equation (16) must also be uniquely determined for both grain boundary and pore surface. As for the free energy parameters, we fix these parameters from the equilibrium solution of the phase field variables across a flat interface. The relevant details are presented in the [appendix](#). According to the analysis included therein, the free energy parameters are related to the material properties as follows:

$$\gamma^{\text{gb}} = \frac{2}{\sqrt{3}} \sqrt{C \kappa_\eta}, \quad (17)$$

$$\gamma^{\text{s}} = \frac{\sqrt{2}}{6} \sqrt{\kappa_\rho + \kappa_\eta} \sqrt{B + 7C}, \quad (18)$$

$$\delta = \ell = \sqrt{\frac{4\kappa_\eta}{3C}}, \quad (19)$$

where γ^{gb} , γ^{s} and δ are the grain-boundary energy, surface energy and grain-boundary width, respectively, and ℓ is the diffuse interface width. The analysis thus requires the diffuse interface width to be equal to the grain-boundary width. The above three equations along with $6C/\kappa_\eta = (B + C)/\kappa_\rho$ (see the [appendix](#)) completely fix the free energy functional parameters.

3. Numerical implementation

The model solution is performed here in two dimensions although the model itself is three dimensional. As shown later, the two-dimensional solution captures well the main characteristics of grain growth in porous ceria and as such it seems to be a good first step. Ultimately, however, three-dimensional solutions are required. In solving the kinetic equations of the phase field model, a second-order centered finite difference approximation was utilized for all spatial derivatives and an explicit Euler scheme was used for time derivatives. In all test cases, a 256×256 finite difference grid was used. When the model is applied to CeO_2 , a 512×512 grid was used. Due to the high computational cost associated with the large number of non-conserved order parameters, parallel computing was utilized. In all simulations, the interface includes five mesh points.

For convenience, a non-dimensional version of the kinetic equations (see below) is used. The non-dimensional form was obtained using a reference energy density, ε , and reference length scale, ℓ^* , time scale, t^* . We take $\varepsilon = B$ as a reference energy density, $\ell^* = \sqrt{4\kappa_\eta/3C}$ as a reference length scale, and $t^* = 1/L\varepsilon$ as a reference time scale. The normalized equations are thus given by

$$\frac{\partial \rho}{\partial \tau} = \ell^* \nabla \cdot \left[\frac{M}{L\ell^{*2}} \ell^* \nabla \left(\frac{1}{\varepsilon} \frac{\delta F}{\delta \rho} \right) \right] = \tilde{\nabla} \cdot \left[\tilde{M} \tilde{\nabla} \left(\frac{\delta \tilde{F}}{\delta \rho} \right) \right], \quad (20)$$

$$\frac{\partial \eta_\alpha}{\partial \tau} = - \left[\frac{1}{\varepsilon} \left(\frac{\delta F}{\delta \eta_\alpha} \right) \right] = - \left(\frac{\delta \tilde{F}}{\delta \eta_\alpha} \right). \quad (21)$$

Here, $\tau = t/t^*$ is the non-dimensional time, $\tilde{\nabla} = \ell^* \nabla$ is the non-dimensional del operator and $\tilde{M} = M/L\ell^{*2}$ is the non-dimensional atomic mobility. For all simulations presented here, a periodic boundary condition is considered.

As a test case, we present the effect of varying the parameters of the free energy on the microstructure. It can be seen from equations (17), (18) and (A.26) that different free energy parameters can produce different surface to grain-boundary ratios and, hence, different values of the equilibrium dihedral angle, ϕ . The latter is related to the surface and grain-boundary energies by the Young equation:

$$\gamma^{\text{gb}} = 2\gamma^{\text{s}} \cos \frac{\phi}{2}. \quad (22)$$

Therefore, if we set $B = C$ and $\kappa_\rho = \kappa_\eta/3$, we obtain $\gamma^{\text{s}} = 2\gamma^{\text{gb}}/3$ and $\phi = 83^\circ$, while if we put $B = 5C$ and $\kappa_\rho = \kappa_\eta$, we obtain $\gamma^{\text{s}} = \gamma^{\text{gb}}$ and $\phi = 120^\circ$. These results are demonstrated in figure 1.

4. Results and discussion

4.1. Test results

For the sake of illustrating the capability of the model in capturing the microstructure evolution during grain growth, we study the classical example of the grain growth during the sintering of two unequal-sized grains. We then elaborate on the effect of porosity on the kinetics of grain growth in ceramics with CeO_2 taken as a case study. We alert the reader to the fact that, for the material system we studied here, and based on compilation of relevant data, it was determined that the bulk and grain-boundary diffusion mechanisms have much less influence on grain growth compared with the grain-boundary mobility and pore-surface diffusion. As such, the bulk and grain-boundary mechanisms were neglected in this study.

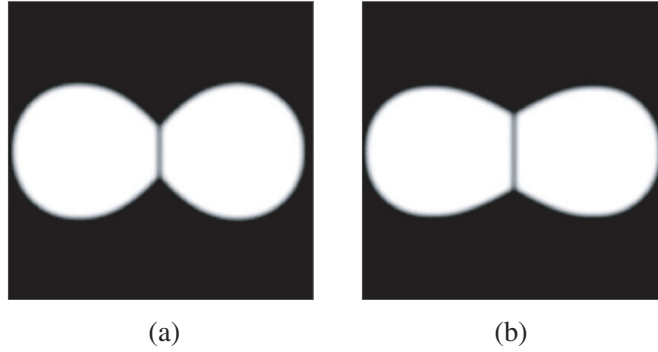


Figure 1. Equilibrium dihedral angles generated using two different sets of free energy parameters: (a) $B = C$ and $\kappa_\rho = \kappa_\eta/3$ give rise to $\phi = 83^\circ$, while (b) $B = 5C$ and $\kappa_\rho = \kappa_\eta$ give $\phi = 120^\circ$.

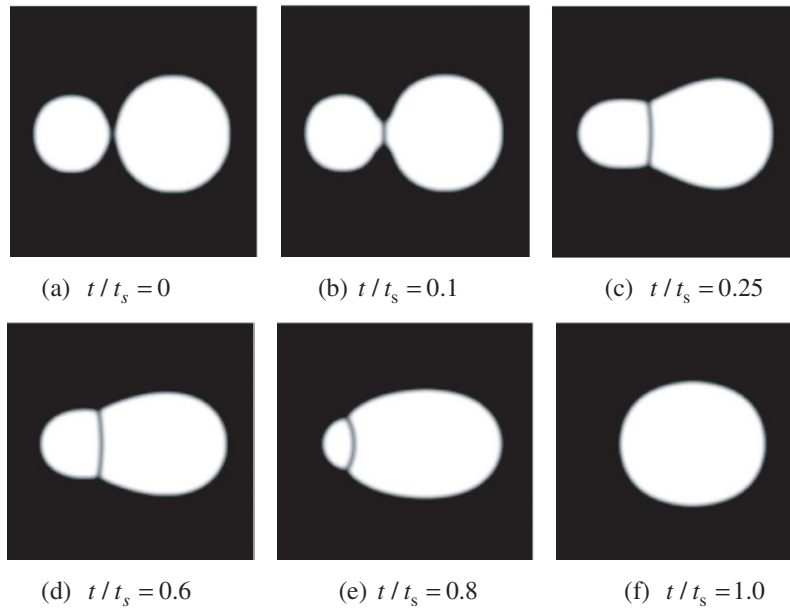


Figure 2. Snapshots of the evolution of a system of two unequal circular grains illustrating the stages of neck formation, concurrent widening of the neck and growth of the larger grain and the final neck shrinkage and complete disappearance of the smaller grain.

Consider two barely touching circular grains as depicted in figure 2. The small grain has a radius of 20 grid points or pixels while the large one has a radius of 30 grid points. The evolution of this two-grain system is captured in figure 2. As the figure shows, the neck between the two grains is first formed with the aid of surface diffusion. Then concurrent grain and neck growth is observed. In the final stage, grain growth proceeds until the equilibrium configuration of one circular grain is established. In this simulation, we set $B = 11C$ and $\kappa_\rho = 2\kappa_\eta$, and the ratio of Cahn–Hilliard to Allen–Cahn mobility was set to 10. The radius of the small grain and the neck (now the grain boundary) size were used as indicators of the extent of system evolution. The area of each grain is calculated as $\int \eta_i dA$ while the neck size was approximated by the product $\eta_1 \times \eta_2$, which has non-zero value only at the neck (grain boundary). The evolution time is presented as a fraction of the total simulation time, t_s .

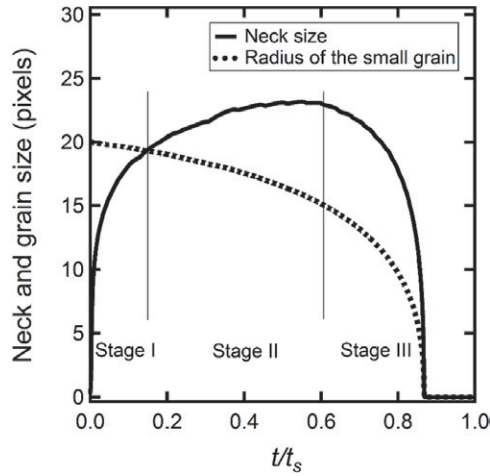


Figure 3. Different stages of sintering of two unequal circular grains; neck formation and growth dominate the initial stage, concurrent grain and neck growth mark the intermediate stage, and the small grain completely disappears in the final stage.

These quantitative results are presented in figure 3. As can be seen in figure 3, the overall evolution process can be divided into three stages. In the first stage, the neck (grain boundary) between the two grains grows quickly without any noticeable change in the grain size. In the second stage, there is a concurrent neck growth and grain growth or shrinkage (the large grain grows while the small grain shrinks). In the third stage, the grain growth or shrinkage continues but the neck size starts to decrease. The final stage continues until the small grain ceases to exist.

The above example illustrates the competition between sintering (neck growth) and grain growth, which can be explained by comparing the driving forces for the two processes. The chemical potentials for neck growth, $\Delta\mu_n$, and grain growth, $\Delta\mu_{gg}$, can be estimated as follows:

$$\Delta\mu_n = \gamma^s v_m \left(\frac{1}{r_n} - \frac{1}{R_i} \right), \quad (23)$$

$$\Delta\mu_{gg} = \gamma^{gb} v_m \left(\frac{1}{R_l} - \frac{1}{R_s} \right). \quad (24)$$

In the above, r_n is the neck radius of curvature, R_i is the radius of curvature of either particle (grain), R_s and R_l refer to the radii of curvature of the small and the large particle, respectively. Since the neck radius of curvature is initially small and negative relative to the larger and positive radii of curvature of the particles, the chemical potential for neck growth is orders of magnitude higher than that of grain growth, and hence the neck growth dominates the first stage. As the neck size grows, the neck radius of curvature increases and hence the chemical potentials become of the same order of magnitude. This is manifested in the second stage where neck growth and grain growth occur simultaneously. The second stage terminates when the increase in the grain-boundary area at the expense of the decrease in the surface area is no longer energetically favorable. In the third stage, the system can decrease its free energy only by decreasing the grain-boundary energy, which can be achieved by grain growth. Hence the growth of the larger grain continues and the neck size decreases during this stage. The different stages captured here are similar to what was suggested by Lang [34] in an analytical model and what was obtained by a similar phase field model [35].

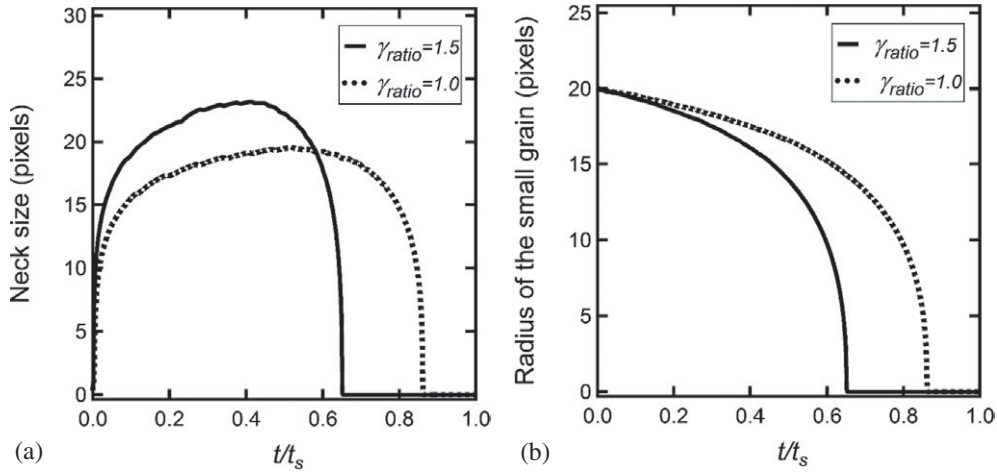


Figure 4. Effect of surface to grain-boundary energy ratio, $\gamma_{ratio} = \gamma^s / \gamma^{gb}$, on (a) neck growth and (b) grain growth. As the surface energy increases, the neck formation and growth become much faster and the grain coalescence is accelerated.

As can be expected from equations (23) and (24), the surface and grain-boundary energies affect the rates of the neck and grain growth. Figure 4 shows the effect of surface energy on the overall kinetics. In obtaining this figure, two sets of the free energy parameters, ($B = 5C$, $\kappa_\rho = \kappa_\eta$) and ($B = 11C$, $\kappa_\rho = 2\kappa_\eta$), that give the same grain-boundary energy but different surface energies were used (see equations (17)–(19) and (A.26)). Also, the ratio of Cahn–Hilliard to Allen–Cahn mobility was set to 10 in the simulation. As can be seen in figure 4, increasing the surface energy for a given grain-boundary energy tends to accelerate the process of coalescence of the two grains, and this effect is more pronounced during the first and second stages due to higher driving force for the neck growth.

4.2. Effect of porosity

We now turn attention to the effect of porosity on the grain growth kinetics in polycrystalline solids. The polycrystalline structure is obtained by generating Voronoi diagrams, and each grain is assigned a different order parameter, which prevents unphysical coalescence of grains and captures the correct kinetics of grain growth. Pores are then introduced randomly on grain boundaries to mimic real materials.

The kinetics of grain growth in the presence of porosity is complicated by the interaction of pores and grain boundaries. Two scenarios are usually investigated in this regard [1, 36]. The first is the separation of pores from the boundary and the second is the migration of pores with the boundary. These possibilities can be represented in terms of the pore velocity v_p and the grain-boundary velocity v_b as follows. The pore will be attached to the boundary when $v_p = v_b$ and it will be separated from the boundary when $v_b > v_p$. The pore velocity could be expressed as $v_p = M_p F_p$, where M_p is the pore mobility and F_p is the driving force for pore migration. The grain-boundary velocity is given by $v_b = M_b (F_b - N_p F_p)$. Here M_b is the boundary mobility, F_b is the force on a pore-free boundary due to its curvature and N_p is the number of pores per unit area of grain boundary. Let $Z = F_b / N_p F_p$ be the force ratio and $W = M_p / N_p M_b$ be the mobility ratio. From above, separation will occur if $Z - 1 > W$.

While pore separation is an indication of abnormal grain growth, only normal grain growth is considered here. In the latter case, the pore velocity is the same as the boundary velocity

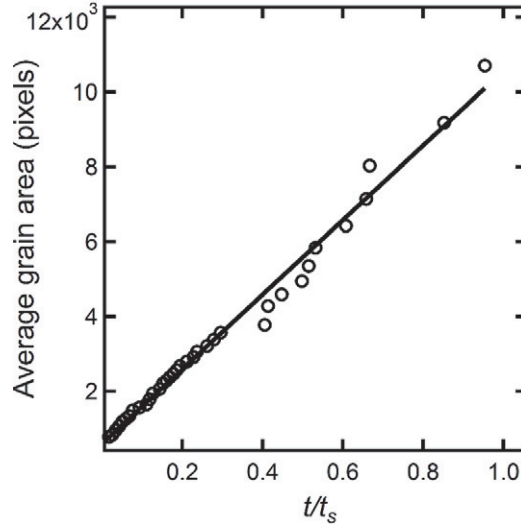


Figure 5. Kinetics of boundary controlled grain growth ($\tilde{M}^s = 8$, $N_p = 0.08$ and $f = 0.02$). A linear relation for the evolution of the average grain area was observed indicating the negligible pore effect. The circles are the data points and the solid line represents a linear fit for the data.

and both are given by

$$v_b = v_p = V = \frac{W}{W+1} M_b F_b. \quad (25)$$

Two limiting cases can be considered from the above equation, $W \gg 1$ and $W \ll 1$. The first limit implies that the pore mobility is much greater than the boundary mobility, which yields $V = M_b F_b$, i.e. the pores have negligible effect on the boundary velocity. This case is referred to as boundary controlled grain growth. In the second limit the boundary mobility is much greater than the pore mobility, and this implies that $V = W M_b F_b = M_p F_b / N_p$. This case is referred to as pore controlled growth. It was shown that the kinetics of pore controlled grain growth follows a power law with an exponent determined by the dominant mechanism for pore migration [1]. In the context of our model, these growth criteria could be stated as follows: growth will be pore controlled if $\tilde{M} \ll N_p$ (see equations (20) and (21)) and boundary controlled if $\tilde{M} \gg N_p$. In our analysis, N_p is calculated as the ratio of the pore area to grain-boundary area and \tilde{M} is a non-dimensional mobility. Moreover, in all cases presented here, the pore volume fraction f will be given in conjunction with N_p since the volume fraction is usually the pore measure mentioned in experiments.

In investigating such scenarios, a set of free energy parameters, $B = 11C$ and $\kappa_\rho = 2\kappa_\eta$, was chosen such that the ratio of the surface to grain-boundary energy is 1.5. Again for all cases considered here, the time is represented as a fraction of the total simulation time and the latter was the same for all tests. For the boundary controlled growth case, the following parameters were used: $\tilde{M}^s = 8.0$, $N_p = 0.08$ and $f = 0.02$. Here we express the atomic mobility in terms of surface mobility since the latter is the fastest mechanism. As expected, the grain growth kinetics follows the well-known parabolic law. This is captured in figure 5, which shows that the evolution of the average grain area, A , is linearly dependent on time. The data were fit to the following equation:

$$A = A_0 + kt. \quad (26)$$

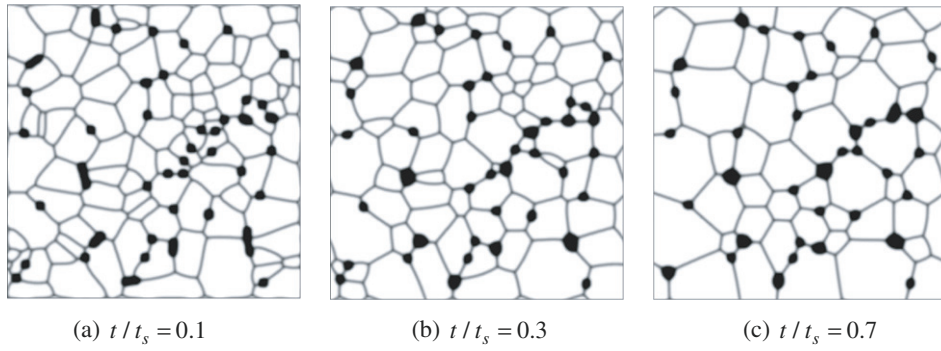


Figure 6. Microstructure evolution during boundary controlled growth ($\tilde{M}^s = 8$, $N_p = 0.08$ and $f = 0.02$). Simultaneous pore coalescence and grain growth are evident.

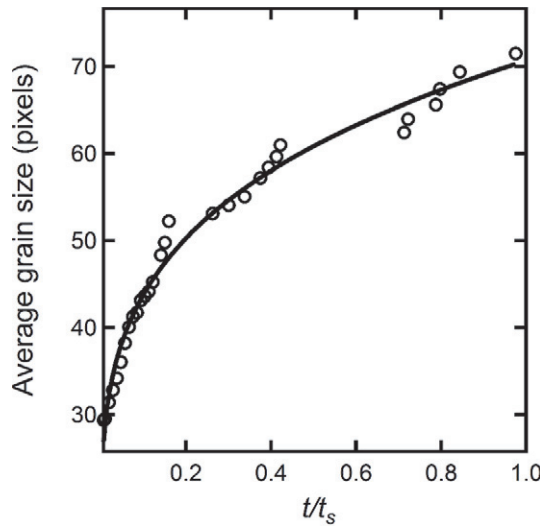


Figure 7. Kinetics of pore controlled grain growth ($\tilde{M}^s = 10^{-3}$, $N_p = 0.1$ and $f = 0.025$). The evolution of the average grain size is described by a power law with exponent of 4, indicating the profound effect of pores on the grain growth. The exponent value is consistent with pore migration by surface diffusion.

Here A_0 is the average initial grain area and k is the rate constant. For the example depicted in figure 5, $A_0 = 598.81$ and $k = 95.024$. It is worth noting that the model captures pore coalescence simultaneously with grain growth. This is most evident from figure 6 where the average pore area increases while the number of pores decreases. Pore coalescence during the sintering of porous solids has been seen in experiments [1, 3] and it is attributed to the fact that the system lowers its free energy by either decreasing its interfacial energy via grain growth or by decreasing its surface energy via pore coalescence.

Pore controlled growth occurs at a larger pore volume fraction. A test case is considered in which $\tilde{M}^s = 10^{-3}$, $N_p = 0.1$ and $f = 0.025$, and the resulting kinetics are shown in figure 7. In this case, the evolution of the average grain size is best described by a power law with exponent determined by the diffusion mechanism that dominates the pore migration. The data were best fit to a power law of the form

$$D^n - D_0^n = kt. \quad (27)$$

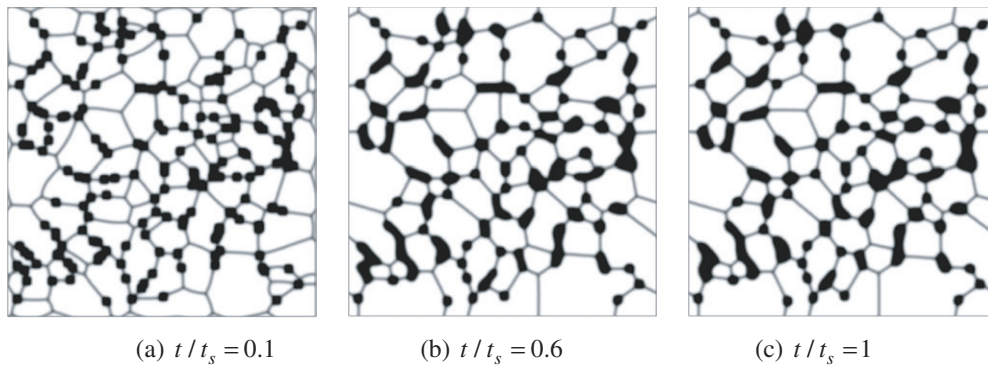


Figure 8. Snapshots of microstructure evolution during pore controlled grain growth ($\tilde{M}^s = 10^{-3}$, $N_p = 0.4$ and $f = 0.1$). Grain growth ceases at half the simulation time.

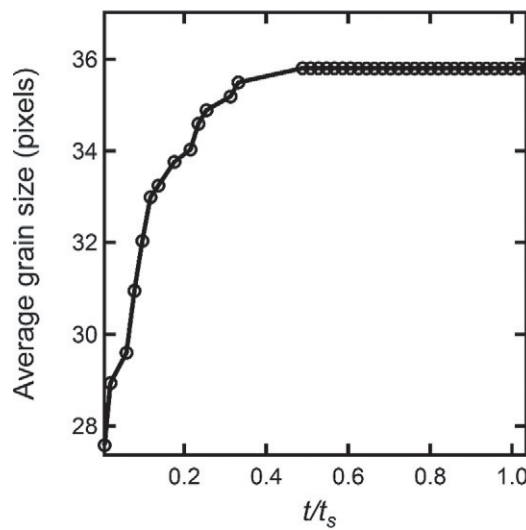


Figure 9. Effect of pore fraction on pore controlled grain growth ($\tilde{M}^s = 10^{-3}$, $N_p = 0.4$ and $f = 0.1$). High pore fraction hinders grain-boundary migration to the degree that grain growth stops. A limiting grain size of 36 pixels was reached at half the simulation time.

In the above, D is the average grain size, D_0 is the initial grain size and k is the rate constant. For the example considered here, it is found that $k = 27.52$ and $n = 4$. The exponent value of 4 agrees well with the theoretical value for pore migration by surface diffusion [1], which is the faster mechanism here.

In the case of pore controlled growth, it is expected that the pore fraction could have a pronounced effect on the process. Recall that in the pore controlled case, $V = M_p F_b / N_p$. The effect of pore fraction was examined using a pore volume fraction of 0.1 along with the same value of surface mobility used above for the pore control case. Increasing the porosity strongly inhibits grain-boundary migration to the degree that grain growth may cease to exist (a Zener-like limit). This is depicted by the snapshots shown in figures 8, which clearly show that the microstructure does not change much after half of the total simulation time (compare figures 8(b) and (c)). This behavior is further illustrated in figure 9 where a limiting grain size was reached at half the total simulation time. Experimental work on ceramics such as UO_2

Table 1. List of impurities in the 99.9% pure CeO₂ used in this work.

Impurity	Cr ₂ O ₃	Nd ₂ O ₃	Eu ₂ O ₃	Fe ₂ O ₃	Na ₂ O ₃	Pr ₆ O ₁₁	Sm ₂ O ₃	Yb ₂ O ₃
Maximum content (ppm)	10	50	50	10	50	50	50	10

captured the development of a limiting grain size at which the grain growth ceases [37]. We interpret the Zener-like limit mentioned here as an equilibrium state in which the capillary effects of pore surface and grain boundary lock the system in place.

4.3. Model application to CeO₂

Here we have chosen grain growth in ceria as our case study. There are contradicting results regarding the kinetics of grain growth in CeO₂. For example, Chen and Chen [38] have reported parabolic grain growth even when dopants are present, while the results obtained by Zhang *et al* [39] suggested different kinetics that is best described by a power law. Zhang *et al* [39] argued that the differences may be due to the different methods by which the powder was prepared. Here we demonstrate that the different values for the exponent stem from the different amounts of initial porosity in the samples used for grain growth studies. This is consistent with Zhang's argument since each preparation method usually gives different values for the relative density or porosity.

We have carried out an experiment to obtain a new data set on grain growth in CeO₂. Bulk ceria pellets were sourced from Alpha Aesar with a density of 6.9 g cm⁻³ and a purity of 99.9%, with the impurities listed in table 1. The pellets were sectioned into discs 3 mm in diameter and 1 mm thick. Subsequently, samples were annealed in a tube furnace under ambient atmospheric condition, and at temperatures of 1400 or 1600 °C for times of 5, 10 and 15 h. After annealing, SEM images of randomized areas for all samples, including the as-received sample, were captured. Magnification levels were chosen such that images included at least 50 grains to produce statistically sound results following average grain size calculation. The Automatic Image Analysis Procedure, described in ASTM Standard E1382-R10 [40], was used to calculate the average grain size based on the number of whole grains within a known rectangular area. Five images, one from each of five different locations, for each condition were analyzed and the measured average and standard deviation were calculated. Figure 10 shows the microstructures of the samples annealed at 1600 °C for 5 and 10 h compared with the as-received microstructure. The images shown are representative for each condition. Figure 11 shows a graphical representation of the time evolution of the measured grain sizes. The grain size of CeO₂ was observed to have grown from its as-received state of 5.19 ± 2.40 to 5.42 ± 2.58 μm after annealing at 1400 °C for 15 h, and to 24.52 ± 11.88 μm after annealing at 1600 °C for 15 h.

The as-received CeO₂ has a standard deviation that is almost half of the average grain size, and a large distribution of sizes can be seen in figure 10(a). Upon annealing at 1600 °C, there appears to be a plateau in grain growth between 10 and 15 h (see figure 11); however, the standard deviation for the average grain size continues to increase with annealing time. This is typical in situations where abnormal grain growth occurs [1]. Another indication of abnormal grain growth is the appearance of voids within grains after they break away from the grain boundaries [1].

The grain growth data at 1400 °C can hardly be used to make quantitative statements about the nature of the growth law in CeO₂ because the average grain size did not change appreciably over the annealing interval and the spread in the grain size is too close to the average grain size itself to enable meaningful measurements. The grain growth data at 1600 °C, however, seem

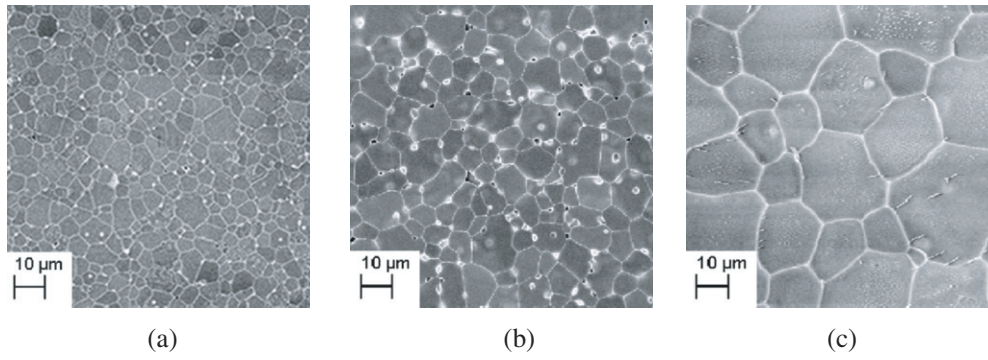


Figure 10. Scanning electron microscopy images of as-received and annealed ceria: (a) as-received, (b) annealed at 1600 °C for 5 h and (c) annealed at 1600 °C for 10 h.

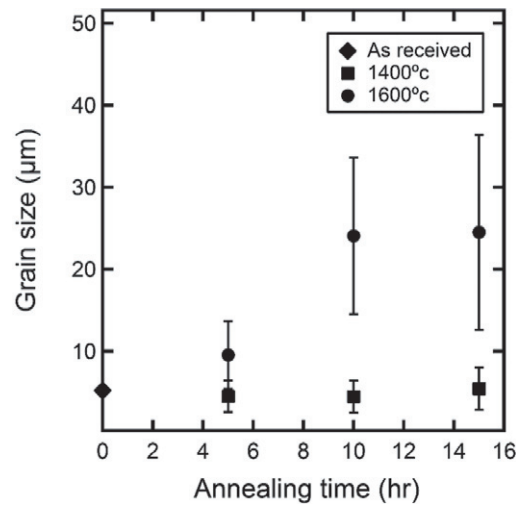


Figure 11. Evolution of grain size for CeO₂ samples annealed at 1400 and 1600 °C.

to follow a power law. Analysis of the data showed that they are best fit by an exponent slightly below 2, which indicates the possibility of a growth mechanism in the material which has not been considered before. The connection between the model predictions and experimental data will thus be made with the earlier literature [38]. The growth data shown in figure 11, however, represent a peculiarity of grain growth to be resolved in the future as further search for growth mechanisms in complex materials such as ceria continues.

In applying our model to CeO₂, surface and grain-boundary energies of ceria were taken to be 1.5 and 1.0 J m⁻², respectively [41]. Referring to equations (17)–(19) and (A.26) and assuming a grain-boundary width of 2 nm, the free energy parameters were determined to be $B = 4.125 \times 10^9 \text{ J m}^{-3}$, $C = 3.75 \times 10^8 \text{ J m}^{-3}$, $\kappa_\eta = 2 \times 10^{-9} \text{ J m}^{-1}$ and $\kappa_\rho = 4 \times 10^{-9} \text{ J m}^{-1}$. The surface diffusion coefficient is directly taken from [41]. According to the analysis given by Allen [33], the Allen–Cahn mobility, which is considered here as the pore-free grain-boundary mobility, can be directly estimated from the relationship: $\kappa_\eta L = \gamma^{gb} M_b$, and the grain-boundary mobility, M_b , of ceria was obtained from [38].

When solving the phase field kinetic equations, numerical stability requires a few mesh points to be placed within the interfacial regions. Since the physical interface width is

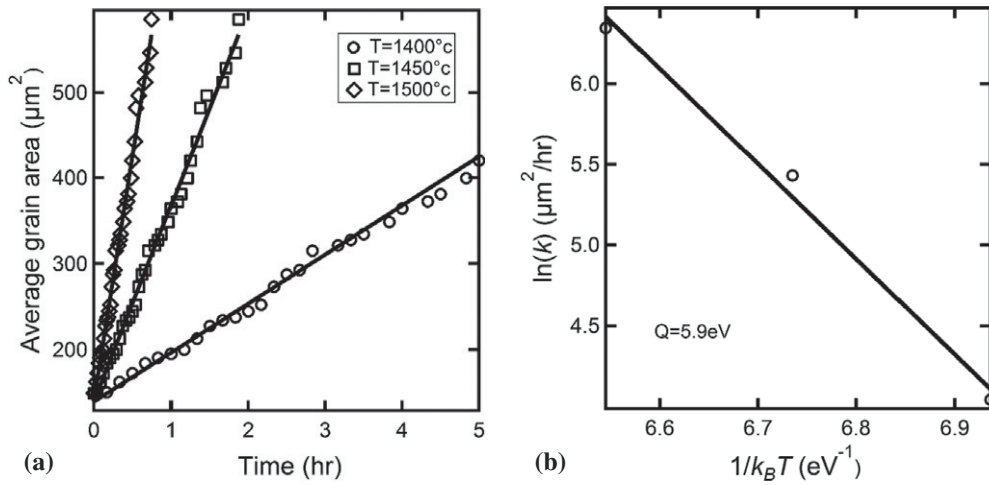


Figure 12. Kinetics of grain growth in fully dense CeO_2 : (a) the linear growth for the average area indicates boundary controlled kinetics and (b) an Arrhenius plot for the rate constant showing an activation energy of 5.9 eV.

in nanometers, the grid spacing would be limited to about 1 nm. In this case, mesoscale simulations (with grain sizes in micrometers) will not be feasible. This model stiffness can be handled by selecting the value of the diffuse interface large enough; this alters the phase field model parameters without actually altering the thermodynamic driving forces or the kinetics [42–44].

For the simulations of ceria, a domain size of 512×512 grid points, which corresponds to a physical system size of $128 \times 128 \mu\text{m}^2$, with 120 grains was used. First, we study the grain growth in fully dense (non-porous) ceria. The kinetics of grain growth in this case is presented in figure 12(a), which shows the evolution of average grain area at different temperatures. The kinetics of grain growth in non-porous ceria follows a regular parabolic grain growth law for the grain diameter, or a linear growth law for average growth area. The effect of temperature was incorporated into the model through the dependence of the surface diffusion coefficient [41] and grain-boundary mobility [38] on temperature. It is to be noted here that the bulk and grain-boundary diffusion are neglected in the case of fully dense ceria. As one may expect, increasing the temperature enhances the kinetic coefficients and hence accelerates the grain growth process. This is quantitatively demonstrated in figure 12(a) where the rate constant (the slope) for the growth process is shown to be highly dependent on temperature. This strong dependence is best described by the well-known Arrhenius relation:

$$k = k_0 \exp(-Q/k_B T), \quad (28)$$

with k being the rate constant, k_0 the pre-exponential factor, Q the activation energy, k_B the Boltzmann constant and T the absolute temperature. An Arrhenius plot of the rate constant versus temperature can thus be used to determine the activation energy for grain growth, which is shown in figure 12(b). An activation energy of 5.9 eV obtained here is in good agreement with the value of 6.16 eV inferred from experimental study of grain growth in dense ceria [38]. It is to be noted that the grain-boundary mobility values used here are actually those documented in [38]. The model must thus yield the same activation energy as in [38]. The minor discrepancy in activation energy may be attributed to the small round off errors in the solution scheme of the phase field model and possibly slight difference in fitting.

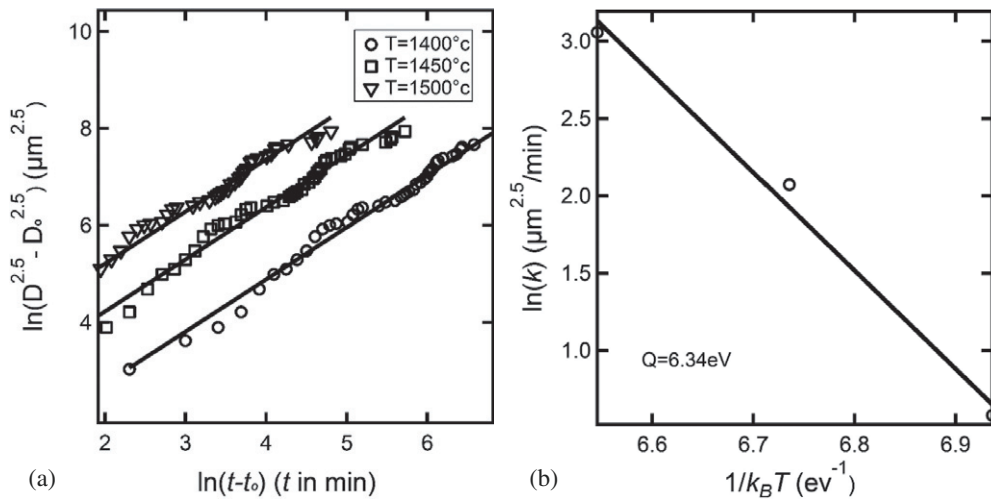


Figure 13. Kinetics of grain growth in CeO_2 with low porosity level ($N_p = 0.04$ and $f = 0.01$). (a) Average grain size growth following a power law with exponent of 2.5. (b) The Arrhenius plot for the rate constant with an activation energy of 6.34 eV.

The effect of porosity on the kinetics of grain growth is investigated by simulating the same polycrystalline structure at the same temperature with different values of pore fraction. Since the presence of pores retards the grain-boundary migration, the overall rate of grain growth decreases with increasing amount of porosity. For a low porosity level, a small deviation from the parabolic grain growth was observed in ceria. This deviation is shown in figure 13(a), which presents the evolution of the average grain size of ceria with 1% porosity level ($N_p = 0.04$ and $f = 0.01$) at different temperatures. At this level of porosity, it was found that the growth is best fit to a power law with exponent of 2.5, compared with 2 as is the case for the grain growth in the fully dense material. This value of growth exponent suggests that there is already a competition between boundary controlled and pore controlled kinetics at such a small level of porosity. Figure 13(a) also shows the effect of temperature on the kinetics of slightly porous ceria. Increasing the temperature tends to increase the rate constant without altering the value of the exponent. The activation energy is calculated from an Arrhenius plot and the result is shown in figure 13(b). At the prescribed porosity level, the activation energy is shown to be 6.34 eV.

As the amount of porosity increases, the grain growth is hindered and the kinetics of growth becomes completely pore controlled. This is demonstrated here by investigating the grain growth in ceria with 4% volume porosity ($N_p = 0.16$ and $f = 0.04$). At this level of porosity, the growth follows a power law with an exponent $n = 4$, which is consistent with pore controlled growth when the dominant mechanism for pore migration is surface diffusion [1]. Figure 14(a) shows the evolution of the average grain size of ceria with 4% porosity at different temperatures. It is evident from the figure that the growth is strongly dependent on temperature. Figure 14(b) shows an Arrhenius plot used to determine the activation energy, which was found to be 6.154 eV.

The observed change of the growth exponent with porosity is natural, and it can help us reconcile the differences in experimental observations of grain growth in ceria [38, 39]. Since the preparation method for obtaining the powder was different in each case, the initial porosity in the samples was different. As the amount of porosity increases in ceria, the grain-boundary

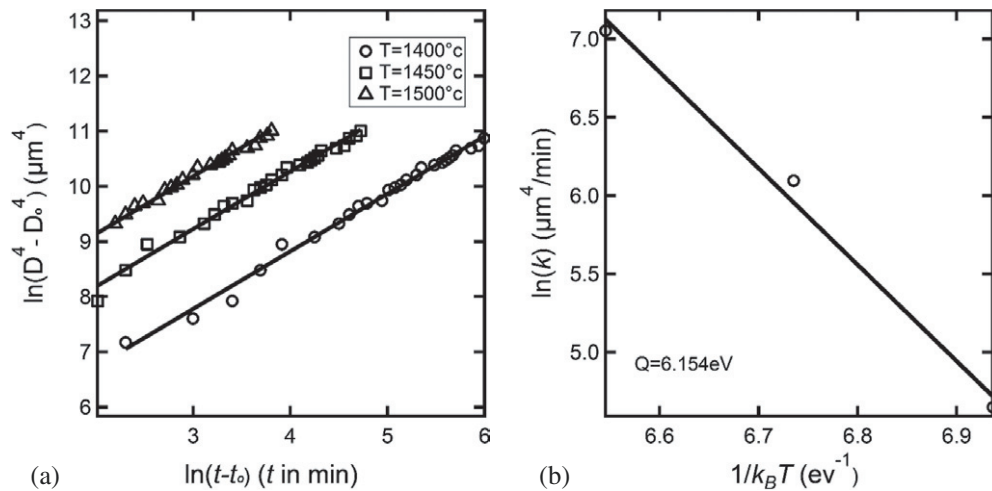


Figure 14. Kinetics of grain growth in CeO_2 with a relatively higher porosity level ($N_p = 0.16$ and $f = 0.04$). (a) Average grain size growth following a power law with exponent of 4, which is indicative of pore controlled growth. (b) The Arrhenius plot for the rate constant with an activation energy of 6.154 eV.

Table 2. The effect of porosity on grain growth in ceria.

Porosity (%)	Exponent	Activation energy (eV)
0	2	5.9
1	2.5	6.34
4	4	6.154

migration is hindered and the growth becomes slower. The effect of porosity on grain growth in ceria is quantitatively expressed in terms of the change of exponent and activation energy with porosity in table 2.

5. Concluding remarks

A phase field model for grain growth in porous polycrystalline ceramics was developed. In addition to grain-boundary migration, the model takes into account surface, grain boundary and volume diffusion to fully account for the effect of pores on the kinetics of the grain growth process. The model parameters were related to thermodynamic and kinetic properties of materials and, hence, quantitative results were obtained, which were compared with experiments. A Voronoi tessellation procedure was used to generate initial polycrystalline structures. Pores were then randomly distributed along the grain-boundary network to mimic real microstructure. A finite difference scheme was used to solve the phase field model equations.

By investigating the classical example of the sintering of two unequal-sized particles, it is shown that the model successfully predicts different stages of sintering in porous polycrystalline solids. In this example, neck formation and growth dominate the initial stage, followed by concurrent neck and grain growth and finally the full coalescence of the two grains. This test demonstrates that the model can be easily applied to powder sintering, a case we will consider in the future. We alert the reader that the term *sintering* here strictly refers to the evolution

of the bonded interfaces. Sintering of a particle aggregate, however, involves densification as well and that is beyond the scope of this paper.

The model has also been shown to capture the experimentally observed features of the grain growth process in porous polycrystalline ceramics. In particular, the simulations demonstrated the concurrent pore coalescence and grain growth in porous polycrystalline systems. For normal grain growth, it is shown that the values of the diffusion coefficients, grain-boundary mobility and pore fraction determine whether the kinetics of grain growth is boundary controlled or pore controlled. In the context of phase field modeling, these growth criteria could be stated as follows: growth will be pore controlled if $M \ll Lr^2N_p$, where M is the Cahn–Hilliard mobility, L is the Allen–Cahn mobility, r is the pore radius and N_p is the fraction of pores per unit grain-boundary area; and it is boundary controlled if $M \gg Lr^2N_p$. A competition between the two different types of kinetics is expected otherwise.

For the boundary controlled grain growth case, the model showed that the average grain size evolution follows the well-known parabolic grain growth law. For the case of pore controlled kinetics, the evolution of the average grain size is best described by a power law with exponent determined by the dominant mechanism for pore migration. Furthermore, the pore fraction was found to have a profound effect on the kinetics of pore controlled grain growth since the presence of pores may hinder the grain-boundary migration to the degree that grain growth will cease, a case that is referred to as the Zener-like limit.

The model application to ceria showed that different values of porosity give rise to different growth exponent values, which is indicative of different types of controlling kinetics. For fully dense ceria, parabolic grain growth was observed and the activation energy obtained here is in good agreement with the corresponding value calculated from experimental data. For slightly porous ceria (1% or less porosity level), a growth exponent of 2.5 was found, which indicates a competition between pore controlled and boundary controlled kinetics. For porosity level of 4% or higher, the grain growth in ceria becomes predominately pore controlled with a growth exponent of 4. This growth exponent value is consistent with pore controlled growth when surface diffusion is the dominant mechanism for pore migration. The growth exponent was found to be independent of temperature; however, the rate constant was shown to be strongly dependent on temperature. This strong dependence was shown to follow the well-known Arrhenius behavior. The analysis of model results in this regard gave activation energies in the range 5.9–6.34 eV, which fall within the experimental range.

The ability to obtain the model parameters in terms of physical materials properties makes this model applicable to real material systems. This proved to be powerful in applying the model to technically important materials such as ceria in the present case. Application of the model to other materials, e.g. uranium dioxide, will be presented elsewhere. By representing the gradient coefficients and Allen–Cahn mobility as functions of the order parameters, the model can be generalized to take into account the effect of anisotropic surface energy, grain-boundary energy and grain-boundary mobility on grain growth [45], which enables the model to study abnormal grain growth.

Acknowledgments

This material is based upon work supported as part of the Center for Materials Science of Nuclear Fuel, an Energy Frontier Research Center funded by the US Department of Energy, Office of Sciences, Office of Basic Energy Sciences under award number FWP 1356, through subcontract number 00122223 at Purdue University. The authors thank Spencer Morris and Jonathan L King, students at the University of Wisconsin, for help with grain data analysis.

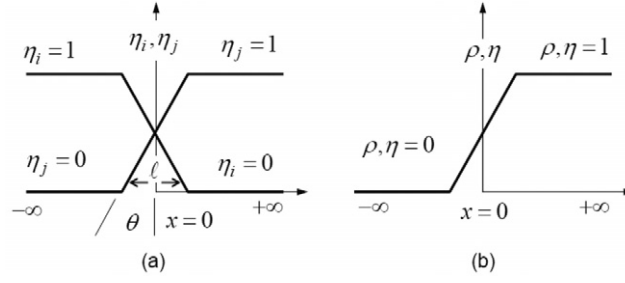


Figure A1. A schematic of the variation of phase field variables across (a) a diffuse flat grain boundary and (b) a diffuse flat surface.

Appendix.

To fix the phase field model parameters, an approach that goes beyond the analyses reported by Moelans and coworkers [45–47] is needed because the current phase field model has two types of interfacial kinetics, pore-surface diffusion and grain-boundary motion. Here, we use the equilibrium solutions of phase field variables to fix the model parameters. We perform this task in two steps. First we study the phase field profiles across a flat grain boundary between two semi-infinite different grains with orientations i and j (see figure A1(a)). Across a grain boundary, the change in the density field is very small, $\rho \approx 1$, and can be neglected. By following the Cahn and Hilliard approach [32], the specific grain-boundary energy, γ^{gb} , is given by the integral

$$\gamma^{\text{gb}} = \int_{-\infty}^{+\infty} f(\rho = 1, \eta_i, \eta_j) + \frac{\kappa_\eta}{2} \left[\left(\frac{d\eta_i}{dx} \right)^2 + \left(\frac{d\eta_j}{dx} \right)^2 \right] dx, \quad (\text{A.1})$$

where an isotropic grain-boundary energy was assumed. This assumption leads to only one gradient coefficient. Here, x is the coordinate perpendicular to the grain boundary and $f(\rho = 1, \eta_i, \eta_j)$ is the bulk free energy density (see equation (2)) at the grain boundary between grain i and grain j , which reads as follows:

$$f(\rho = 1, \eta_i, \eta_j) = C [1 - 4(\eta_i^3 + \eta_j^3) + 3(\eta_i^2 + \eta_j^2)^2]. \quad (\text{A.2})$$

For a grain boundary in local equilibrium, the profiles $\eta_i(x)$ and $\eta_j(x)$ must adopt a shape which minimizes the functional (A.1) and satisfies the following boundary conditions (see figure A1(a)):

$$\eta_i = 1 \quad \text{and} \quad \eta_j = 0 \quad \text{for } x \rightarrow -\infty, \quad (\text{A.3a})$$

$$\eta_i = 0 \quad \text{and} \quad \eta_j = 1 \quad \text{for } x \rightarrow +\infty, \quad (\text{A.3b})$$

$$\frac{d\eta_i}{dx} = \frac{d\eta_j}{dx} = 0 \quad \text{for } x \rightarrow \pm\infty. \quad (\text{A.3c})$$

According to the principles of calculus of variations, the functions $\eta_i(x)$ and $\eta_j(x)$ that extremize the functional (A.1) must satisfy Euler equations, namely,

$$\frac{\partial f(\rho = 1, \eta_i, \eta_j)}{\partial \eta_i} - \kappa_\eta \frac{d^2 \eta_i}{dx^2} = 0, \quad (\text{A.4a})$$

$$\frac{\partial f(\rho = 1, \eta_i, \eta_j)}{\partial \eta_j} - \kappa_\eta \frac{d^2 \eta_j}{dx^2} = 0. \quad (\text{A.4b})$$

Equivalently, these profiles satisfy

$$f(\rho = 1, \eta_i, \eta_j) - \frac{\kappa_\eta}{2} \left[\left(\frac{d\eta_i}{dx} \right)^2 + \left(\frac{d\eta_j}{dx} \right)^2 \right] = 0, \quad (\text{A.5})$$

where the boundary conditions (A.3a)–(A.3c) were taken into account. Across a flat grain boundary, and assuming a linear profile of the phase field variable, the following relation holds (see figure A1(a)):

$$\frac{d\eta_j}{dx} \propto -\frac{d\eta_i}{dx}, \quad (\text{A.6})$$

by integrating the above equation taking into account the boundary conditions, we simply obtain

$$\eta_j(x) = 1 - \eta_i(x), \quad (\text{A.7})$$

which is readily seen from figure A1(a). This immediately modifies equation (A.6) to

$$\frac{d\eta_j}{dx} = -\frac{d\eta_i}{dx}, \quad (\text{A.8})$$

which also gives

$$\frac{d\eta_j}{d\eta_i} = -1. \quad (\text{A.9})$$

Rearranging equation (A.5) while taking into account equations (A.7) through (A.9) and the boundary conditions, we obtain

$$\frac{d\eta_i}{dx} = -\sqrt{\frac{f(\rho = 1, \eta_i, \eta_j)}{\kappa_\eta}}, \quad (\text{A.10})$$

$$\frac{d\eta_j}{dx} = \sqrt{\frac{f(\rho = 1, \eta_i, \eta_j)}{\kappa_\eta}}. \quad (\text{A.11})$$

The above two equations are needed to carry out the integral in (A.12), which comes by substituting equation (A.5) into equation (A.1).

$$\gamma^{\text{gb}} = \int_{-\infty}^{+\infty} 2f(\rho = 1, \eta_i, \eta_j) dx. \quad (\text{A.12})$$

From equation (A.7) we have $\eta_j(x) = 1 - \eta_i(x)$, so by substituting this relation into equation (A.2) and skipping some algebraic details we obtain

$$f(\rho = 1, \eta_i, \eta_j = 1 - \eta_i) = f(\eta_i) = 12C\eta_i^2(1 - \eta_i)^2. \quad (\text{A.13})$$

Substituting by equation (A.10) and equation (A.13) into equation (A.12) gives

$$\gamma^{\text{gb}} = 2\sqrt{12C\kappa_\eta} \int_0^1 \eta_i (1 - \eta_i) d\eta_i = \frac{2}{\sqrt{3}} \sqrt{C\kappa_\eta}. \quad (\text{A.14})$$

Equation (A.14) establishes a direct relation between two of the model parameters and a material property which is the specific grain-boundary energy.

The diffuse interface width across a flat grain boundary can be estimated from the model parameters by (see figure A1(a))

$$\left(\frac{d\eta_j}{dx}\right)_{x=0} = \tan \theta = \frac{1}{\ell}. \quad (\text{A.15})$$

From equations (A.11) and (A.13) and figure A1(a), we have

$$\left(\frac{d\eta_j}{dx}\right)_{x=0} = \sqrt{\frac{f(\eta_i = 0.5)}{\kappa_\eta}} = \sqrt{\frac{3C}{4\kappa_\eta}}. \quad (\text{A.16})$$

The last two relationships yield

$$\ell = \sqrt{\frac{4\kappa_\eta}{3C}} = \delta, \quad (\text{A.17})$$

where δ is the grain-boundary thickness. Equation (A.17) provides a relation between the model parameters and another material property which is the grain-boundary thickness.

There are still two parameters in the free energy functional to be determined, B and κ_ρ . These parameters can be obtained from the phase field profiles in equilibrium across a flat free surface. Without loss of generality, we consider the phase field profiles across a flat free surface at $x = 0$ between a semi-infinite solid grain and semi-infinite amorphous/pore phase (see figure A1(b)). In this case, both fields change across the interface and hence the specific surface energy is calculated from the integral

$$\gamma^s = \int_{-\infty}^{+\infty} f(\rho, \eta) + \frac{\kappa_\rho}{2} \left(\frac{d\rho}{dx}\right)^2 + \frac{\kappa_\eta}{2} \left(\frac{d\eta}{dx}\right)^2 dx. \quad (\text{A.18})$$

Here $f(\rho, \eta)$ is the bulk free energy density (see equation (2)) when only one solid grain is present,

$$f(\rho, \eta) = B\rho^2(1 - \rho)^2 + C[\rho^2 + 6(1 - \rho)\eta^2 - 4(2 - \rho)\eta^3 + 3\eta^4]. \quad (\text{A.19})$$

At equilibrium, the functional (A.18) must be a minimum which requires

$$\frac{\partial f(\rho, \eta)}{\partial \eta} - \kappa_\eta \left(\frac{d^2\eta}{dx^2}\right) = 0, \quad (\text{A.20a})$$

$$\frac{\partial f(\rho, \eta)}{\partial \rho} - \kappa_\rho \left(\frac{d^2\rho}{dx^2}\right) = 0. \quad (\text{A.20b})$$

Upon integration, the above two equations yield

$$f(\rho, \eta) - \left[\frac{\kappa_\eta}{2} \left(\frac{d\eta}{dx}\right)^2 + \frac{\kappa_\rho}{2} \left(\frac{d\rho}{dx}\right)^2 \right] = 0, \quad (\text{A.21})$$

where the boundary conditions $\rho(\infty) = \eta(\infty) = 1$ and $\rho(-\infty) = \eta(-\infty) = 0$ were used. From figure A1(b), one expects the following relation to be valid:

$$\frac{d\eta}{dx} \propto \frac{d\rho}{dx}, \quad (\text{A.22})$$

which, after applying the boundary conditions above, gives

$$\rho(x) = \eta(x). \quad (\text{A.23})$$

From the last equation one obtains

$$\frac{d\eta}{dx} = \frac{d\rho}{dx} \quad (\text{A.24})$$

and

$$f(\rho, \eta = \rho) = f(\rho) = (B + 7C)\rho^2(1 - \rho)^2. \quad (\text{A.25})$$

According to Euler equations (A.20), such relations are valid only if $(1/\kappa_\rho)\partial f/\partial \rho = (1/\kappa_\eta)\partial f/\partial \eta$, which holds if the following relation holds:

$$\frac{6C}{\kappa_\eta} = \frac{B + C}{\kappa_\rho}. \quad (\text{A.26})$$

Following the procedure leading to equation (A.14) for obtaining the grain-boundary energy, the surface energy is finally found to be

$$\gamma^s = \frac{\sqrt{2}}{6} \sqrt{\kappa_\rho + \kappa_\eta} \sqrt{B + 7C}. \quad (\text{A.27})$$

Equations (A.14), (A.17), (A.26) and (A.27) uniquely fix the unknown free energy parameters B , C , κ_ρ and κ_η in terms of the surface energy, grain-boundary energy and grain-boundary width for any particular material.

References

- [1] Rahaman M N 2003 *Ceramic Processing and Sintering* (New York: Dekker)
- [2] Burke J E and Turnbull D 1952 *Prog. Met. Phys.* **3** 220
- [3] Kingery W D, Bowen H K and Uhlmann D R 1976 *Introduction to Ceramics* (New York: Wiley)
- [4] Anderson M P, Srolovitz D J, Grest G S and Shan P S 1984 *Acta Metall.* **32** 783
- [5] Srolovitz D J, Anderson M P, Shan P S and Grest G S 1984 *Acta Metall.* **32** 793
- [6] Saito Y 1997 *Mater. Sci. Eng. A* **223** 114
- [7] Xiaoyan S, Guoquan L and Nanju G 2000 *Scr. Mater.* **43** 355
- [8] Wang C and Lui G 2003 *Mater. Lett.* **57** 4424–8
- [9] Frost H G, Thompson C V, Howe C L and Whang J 1988 *Scr. Metall.* **22** 65
- [10] Fayad W, Thompson C V and Frost H G 1999 *Scr. Metall.* **40** 1199
- [11] Gill S P A and Cocks A C F 1996 *Acta Mater.* **44** 4777
- [12] Cleri F 2000 *Physica A* **282** 339
- [13] Moldovan D, Wolf D, Phillpot S R and Haslam A J 2002 *Acta Mater.* **50** 3397
- [14] Moldovan D, Wolf D, Phillpot S R and Haslam A J 2002 *Phil. Mag. A* **82** 1271
- [15] Fuchizaki K and Kawasaki K 1995 *Physica A* **221** 202
- [16] Liu Y, Baudin T and Penelle R 1996 *Scr. Mater.* **34** 1679
- [17] Geiger J, Roos A and Barkoczy P 2001 *Acta Mater.* **49** 623
- [18] Chen L Q and Yang W 1994 *Phys. Rev. B* **50** 15752
- [19] Fan D, Geng C and Chen L Q 1997 *Acta Mater.* **45** 1115
- [20] Kazaryan A, Wang Y, Dregia S A and Patton B R 2001 *Phys. Rev. B* **63** 184102
- [21] Kazaryan A, Wang Y, Dregia S A and Patton B R 2002 *Acta Mater.* **50** 2491
- [22] Kazaryan A, Patton B R, Dregia S A and Wang Y 2002 *Acta Mater.* **50** 499
- [23] Doherty R D, Srolovitz D J, Rollett A D and Anderson M P 1987 *Scr. Metall.* **21** 675
- [24] Anderson M P, Grest G S, Doherty R D, Li K and Srolovitz D J 1989 *Scr. Metall.* **23** 753
- [25] Fan D, Chen L Q and Chen S P 1998 *J. Am. Ceram. Soc.* **81** 526
- [26] Edelson L H and Glaeser A M 1988 *J. Am. Ceram. Soc.* **71** 225
- [27] Hayun S, Shavareva T Y and Navrotsky A 2011 *J. Am. Ceram. Soc.* **94** 3992
- [28] Mihalache V and Pasuk I 2011 *Acta Mater.* **59** 4875
- [29] Landau L D and Lifshitz E M 1980 *Statistical Physics* (Oxford: Pergamon)
- [30] Wang Y 2006 *Acta Mater.* **54** 953
- [31] Gugenberger C, Spatschek R and Kassner K 2008 *Phys. Rev. E* **78** 016703
- [32] Cahn J W 1961 *Acta Metall.* **9** 795
- [33] Allen S M and Cahn J W 1979 *Acta Metall.* **27** 1085
- [34] Lange F F and Kellett B J 1989 *J. Am. Ceram. Soc.* **72** 735
- [35] Kumar V, Fang Z Z and Fife P C 2010 *Mater. Sci. Eng. A* **528** 254
- [36] Brook R J 1969 *J. Am. Ceram. Soc.* **52** 56
- [37] Ainscough J B, Oldfield B W and Ware J O 1973 *J. Nucl. Mater.* **49** 117

- [38] Chen P and Chen I 1996 *J. Am. Ceram. Soc.* **79** 1793
- [39] Zhang T S, Ma J, Kong L B, Zeng Z Q, Hing P and Kliner J A 2003 *Mater. Sci. Eng. B* **103** 177
- [40] ASTM E112-10 2010 *Standard Test Method for Determining Average Grain Size* (West Conshohocken, PA: ASTM International)
- [41] Zouvelou N, Mantzouris X and Nikolopoulos P 2008 *Mater. Sci. Eng. A* **495** 54
- [42] Chen Q, Ma N, Wu K and Wang Y 2004 *Scr. Mater.* **50** 471
- [43] Shen C, Chen Q, Wen Y H, Simmons J P and Wang Y 2004 *Scr. Mater.* **50** 1023
- [44] Shen C, Chen Q, Wen Y H, Simmons J P and Wang Y 2004 *Scr. Mater.* **50** 1029
- [45] Moelans N, Blanpain B and Wollants P 2008 *Phys. Rev. B* **78** 024113
- [46] Vanherpe L, Moelans N, Blanpain B and Vandewalle S 2007 *Phys. Rev. E* **76** 056702
- [47] Vanherpe L, Moelans N, Blanpain B and Vandewalle S 2011 *Comput. Mater. Sci.* **50** 2221